6. Chapter 6: Preparation and evaluation of $Ana_{C15:3}$/HP-β-CD inclusion complex

6.1 Materials

Table 6.1: List of chemicals used in the preparation of inclusion complex

S.No	Materials	Supplier
1.	Hydroxypropyl-β-cyclodextrin	Himedia Laboratories, Mumbai.
2.	Live/Dead cell viability kit (Syto 9/Propidium iodide)	Thermo Fischer Scientific, India
3.	Potassium dihydrogen orthophosphate	S D Fine chem limited, Mumbai
4.	Di-sodium hydrogen orthophosphate anhydrous	S D Fine chem limited, Mumbai
5.	Type 1 water (HPLC garde)	Arium ® Pro ultrapure water purification system
6.	Ethanol	Merck Life Science, Mumbai
All other chemicals were of analytical grade		

6.2 Methods

6.2.1 Analytical method

6.2.1.1 Calibration curve of $Ana_{C15:3}$ in ethanol

Stock solution (100 µg/mL) of $Ana_{C15:3}$ was prepared by dissolving 5 mg accurately weighed $Ana_{C15:3}$ in 50 mL ethanol. From the stock solution, 0.1, 0.2, 0.4, 0.6, 0.8, 1, 2 and 3 mL solutions were taken out using micropipette and diluted up to 10 mL with ethanol to finally obtain the concentrations of 1, 2, 4, 6, 8, 10, 20 and 30 µg/mL, respectively. These final solutions were analyzed using a UV-Visible spectrophotometer at 312 nm. Intra and interday precision was also determined.

6.2.1.2 Calibration curve of $Ana_{C15:3}$ in phosphate buffer pH 6.8

Stock solution (100 µg/mL) of $Ana_{C15:3}$ was prepared by dissolving 5 mg accurately weighed Ana ($C_{15:0}$) in 50 mL ethanol. From the stock solution, 0.1, 0.5, 1, 2, 3, 4, and 5 mL solutions were taken out using a micropipette and diluted up to 10 mL with phosphate

buffer to finally obtain the concentrations of 1, 5, 10, 20, 30, 40 and 50 µg/mL respectively. These final solutions were analyzed using a UV-Visible spectrophotometer at 312 nm. Intra and interday precision was also determined.

6.2.2 Preparation of $Ana_{C15:3}$/HP-β-CD inclusion complex

Anacardic Acid Inclusion Complex ($Ana_{C15:3}$ -IC) of molar ratio 1:1 was developed by the co-evaporation method. Briefly, $Ana_{C15:3}$ (87 mg) and HP-β-CD (344 mg) were dissolved completely in ethanol (10 mL) and water (10 mL), respectively. Further, both the solutions were stirred in a sealed glass vial and retained at room temperature with mild stirring for 30 min. The temperature of the mixture was then increased up to 50°C and maintained constant for 2 h while stirring at 500 rpm. Further, the resultant solution was dried by evaporation under low pressure using a rotary evaporator (IKA, Germany) at 40°C to get the final product in the form of solid inclusion complex ($Ana_{C15:3}$ -IC) (Wei, Zhang et al. 2017). $Ana_{C15:3}$ -IC with $Ana_{C15:3}$/HP-β-CD ratio of 0.5:1, 1:2, 1:3, and 1:4 were also prepared using the same technique (Aleem, Kuchekar et al. 2008).

6.2.3 Evaluation of $Ana_{C15:3}$ /HP-β-CD inclusion complex

6.2.3.1 UV–Vis spectroscopy

UV–Visible Spectra of $Ana_{C15:3}$ and $Ana_{C15:3}$-IC was recorded using UV-Visible spectrophotometer (UV-1700 PharmSpec, Shimadzu) with 1 cm quartz cell. The scans were registered in the wavelength range of 210 to 400 nm (Ol'khovich, Sharapova et al. 2017).

6.2.3.2 Solubility study

An excess quantity of $Ana_{C15:3}$ (20 mg) and $Ana_{C15:3}$ /HP-β-CD inclusion complex (100 mg) were added into a glass vial containing 10 mL of water and kept for stirring at temperature 25±0.1°C for 72 h. For solubility determination, both the suspension samples were filtered using a 0.22 µm filter (Millipore syringe filter, PTFE) to separate the

undissolved solid phase followed by suitable dilution with ethanol and UV analysis at λ_{max} 312 nm (Ol'khovich, Sharapova et al. 2017).

6.2.3.3 Phase solubility study

Phase solubility studies of a physical mixture of $Ana_{C15:3}$ and HP-β-CD were conducted as per the previous report (Al-Marzouqi, Shehatta et al. 2006). Briefly, excess quantity (20 mg) of $Ana_{C15:3}$ was mixed with 10 mL of HP-β-CD hydrous solutions with different concentrations (0, 5, 10, 15, 20, 25 mM) followed by ultrasonication for 30 min. The sample suspensions were incubated at a thermal vibrator having a vibration rate of 100 r/min for 72 h at 25°C followed by filtration using 0.22 μm membrane filter (Millipore syringe filter, PTFE) suitable dilution with phosphate buffer (pH 6.8) and analysis by UV spectroscopy at 312 nm. The study was also performed at 35 and 45°C by following the same procedure described above. All the experimental results are expressed in terms of the mean value of the minimum of three repeated experiments (Xu, Zhang et al. 2017). The apparent stability constants (K) were determined using the phase solubility diagrams as per the Higuchi–Connors equation, where S_0 refers to the intrinsic solubility of the solute in the absence of HP-β-CD and slope corresponds to the slope obtained from the phase-solubility plot data from the equation (1). The phase solubility curves were plotted using the molar concentration of HP-β-CD on the X-axis and the molar concentration of $Ana_{C15:3}$ on the Y-axis. The stability constants (K_S) were calculated from phase solubility curves as per the following Higuchi- Conners equation:

$$K = Slope/(S0 \times (1 - Slope)\,) \qquad (1)$$

Where S_0 is the intrinsic solubility of $Ana_{C15:3}$ and slope can be expressed as slope obtained from phase solubility curves.

6.2.3.4 Fourier transform infrared spectroscopy (FT-IR)

The FT-IR spectra of $Ana_{C15:3}$, HP-β-CD, and $Ana_{C15:3}$ /HP-β-CD inclusion complex were obtained using FTIR, Bruker Alpha II FTIR Spectrometer (Bruker Corporation, Germany). The samples were scanned at a spectral range of 500-4000 cm^{-1} with a resolution of 2 cm^{-1} and 128 scans for each run. The samples were first diluted with KBr powder and compressed to form pellets for performing the measurements (Songkro, Hayook et al. 2011).

6.2.3.5 X-ray diffraction (XRD) study

The X-ray diffraction characteristics of the pure compound; $Ana_{C15:3}$, HP-β-CD, and the $Ana_{C15:3}$/HP-β-CD inclusion complexes were examined using Rigaku Miniflex 600 Desktop X-Ray Diffraction system (Rigaku Corporation, Japan) using HyPix-400 MF 2D hybrid pixel array detector (HPAD). The current and voltage applied were 40 mA and 40 kV, respectively. The results were recorded in the 2θ range of 5–40° with scan rate 10°/min and step size 0.03° (Abou-Okeil, Rehan et al. 2018).

6.2.3.6 Differential scanning calorimetry (DSC)

The thermal behavior of the $Ana_{C15:3}$, and inclusion complex was analyzed using a differential scanning calorimeter (DSC-60 Plus, Shimadzu, Japan). The DSC thermograms were recorded in an argon environment (with 99.99% purity) using typical aluminum pans for samples while keeping an empty pan as reference. Samples were weighed accurately into DSC sample pans, hermetically sealed, and heated at a rate of 10°C/min (Nikolic, Savic et al. 2018). The samples were heated, ranging between 25-250°C under a constant nitrogen flow of 100 mL/min.

6.2.3.7 Scanning electron microscopy (SEM)

The morphological investigation of the test samples was carried out using EVO- Scanning Electron Microscope MA15/18 (Carl Zeiss Microscopy Ltd.) equipped with 51N1000 –

Energy Dispersive Spectroscopy (EDS) System (Oxford Instruments Nanoanalysis). The sample preparation involved fixing of sample on a brass stub followed by a thin layer of gold coating to avail good electrical conductivity while performing microscopic scans. Images were recorded at various magnifications (200-2000X) using secondary electrons (SE) to obtain images with good clarity (Duarte, Alves et al. 2015).

6.2.3.8 ^{1}H NMR

Proton (^{1}H) spectra of individual compounds and $Ana_{C15:3}$ /HP-β-CD inclusion complex were recorded using AVH D 500 AVANCE III HD 500 MHz One Bay NMR Spectrometer (Bruker BioSpin International AG, Germany). The test samples were dissolved in dimethyl sulfoxide (DMSO) at 298 ± 0.1 K, and chemical shifts (in ppm) were recorded using tetramethylsilane (TMS) as the internal standard (Xu, Zhang et al. 2017).

6.2.4 Antimicrobial activity

The antimicrobial activity of the $Ana_{C15:3}$ and inclusion complex was assessed by estimating MIC against *S. aureus*. MIC for $Ana_{C15:3}$ and inclusion complex was determined by using the broth dilution method. Microbial suspensions were cultured at 37°C for 24 h and further diluted to produce 1×10^{5} CFU/mL. Further, 20 µL of microbial suspension (1×10^{5} CFU/mL) was mixed with 180 mL Muller Hinton Broth (MHB) comprising different concentrations of $Ana_{C15:3}$ and inclusion complex ranging from 0.097-50 µg/mL in microtiter 96 well plate. The inclusion complex was diluted with the culture media directly, while $Ana_{C15:3}$ was diluted in culture media supplemented with 1% v/v DMSO. Well plates were further incubated at temperature 37°C for 24 h, and further turbidity of the test samples was determined using a microplate reader (MR 680 Bio-Rad) at 450 nm (Nikolic, Savic et al. 2018). The MICs of $Ana_{C15:3}$ and inclusion complex were considered as the minimum concentration with no observable growth (≤ 0.05 difference

in OD 450) examined following the incubation for 24 h. All the experiments were performed in triplicates.

6.2.4.1 Effect of $Ana_{C15:0}$ and $Ana_{C15:0}$-IC on S. aureus biofilms

The biofilm dispersal potential of free $Ana_{C15:3}$ and $Ana_{C15:3}$-IC was determined by using the biofilm developed on the peg lids. Concisely, 96 culture plates (made of Polystyrene, transparent, sterile plates) were plated with 200 µL (0.5×10^6 CFU/mL) of *S. aureus* culture in LB media sheathed with peg lids followed by incubation for 48 h at 37°C on the rotary incubator shaker. The formation of biofilm was further confirmed by methylene blue dye test. Following the 48 h, peg lids having the biofilm were washed with PBS thrice to eliminate the spliced planktonic bacteria, and further, the peg lids containing biofilm were kept over the culture plate (96 well) comprising serially diluted test samples *viz.* 50, 25, 12.5, 6.25, 3.125, 1.562, 0.781, 0.390, 0.195, and 0.097 µg/mL diluted with the LB media. The plates were incubated for 24 h at 37°C, and adhered biofilm was removed by positioning the lid on another 96 well plates comprising fresh LB media followed by sonication (Gade, Patel et al. 2019). The obtained cells were serially diluted and kept on LB agar plates for counting the CFU. Further, the biofilms were treated with a recurrent dose for 72 h to examine the biofilm eradication efficacy of the test samples.

6.2.4.2 Microscopic study of biofilm

Biofilms were developed on the coverslip (12 mm diameter) dipped inside the culture plate (12 well) as per the preceding study. Concisely, coverslips comprising biofilms were recovered from the culture plate after 48 h and gently washed with PBS so as to eliminate the loosely attached bacterial cell. Additionally, the coverslips were relocated to another well plate (12 well) for inducing treatment with various test samples in LB media. Treatment was continued for 24 h followed by removal of coverslips from the well plate. The cells were then fixed with paraformaldehyde (4% w/v), and then cells of the biofilms

were stained using LIVE/DEAD Backlight Bacterial Viability Kit (Thermo Fischer, India) in the dark environment following the manual guidelines (6 µM SYTO 9 and 30 µM Propidium Iodide). The samples were examined using confocal laser scanning microscopy (CLSM) (Zeiss, Germany). The sample sections were scanned at two excitation wavelengths, i.e. 488 and 560 nm employing 40X magnification. The z stack images were acquired at z step size 2.63 µ. Furthermore, the obtained images were analyzed using COMSTAT-2 software to calculate the biomass and thickness of biofilms for different treatment groups (Endo, Costa et al. 2018).

6.3 Results and Discussion

6.3.1 Analytical method

A calibration curve was prepared to calculate $Ana_{C15:3}$ concentrations in the test samples while performing studies like solubility assay, entrapment efficiency determination, and in vitro release. The calibration curves of $Ana_{C15:3}$ were successfully prepared in ethanol (Figure 6.1-A) and phosphate buffer pH 6.8 (Figure 6.1-B) with linearity value (R^2) 0.9995 and 0.9993 respectively.

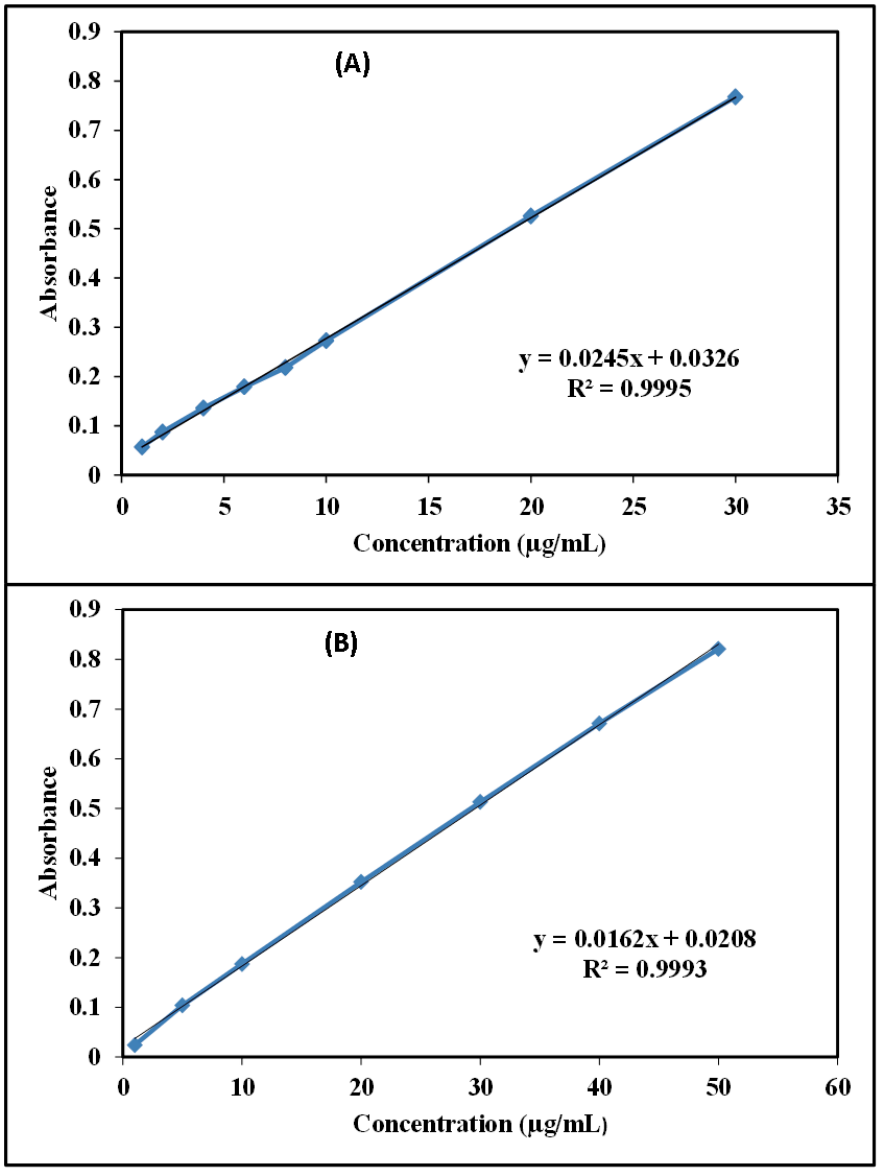

Figure 6.1: Calibration curve of $Ana_{C15:3}$ in ethanol (A) and phosphate buffer pH 6.8 (B) for UV spectrophotometry.

6.3.2 UV–Visible spectroscopy

The UV-Visible spectra of $Ana_{C15:3}$ in phosphate buffer (pH 6.8) having different concentrations of HP-β-CD in the wavelength range of 210–400 nm is shown in Figure 6.2. The UV-spectrum of $Ana_{C15:3}$ in phosphate buffer present bands showing absorption maxima at 243 and 312 nm. The first peak corresponds to the benzene absorption, while another peak indicates a typical pattern of polyphenols. Addition of HP-β-CD in the drug

solution exhibited concentration dependent enhancement in the optical density of $Ana_{C15:3}$ and the bathochromic shift of the absorption bands were observed. This phenomenon demonstrated the non-covalent correlation of $Ana_{C15:3}$ with HP-β-CD and was similar to the earlier reports (Li, Zhang et al. 2005).

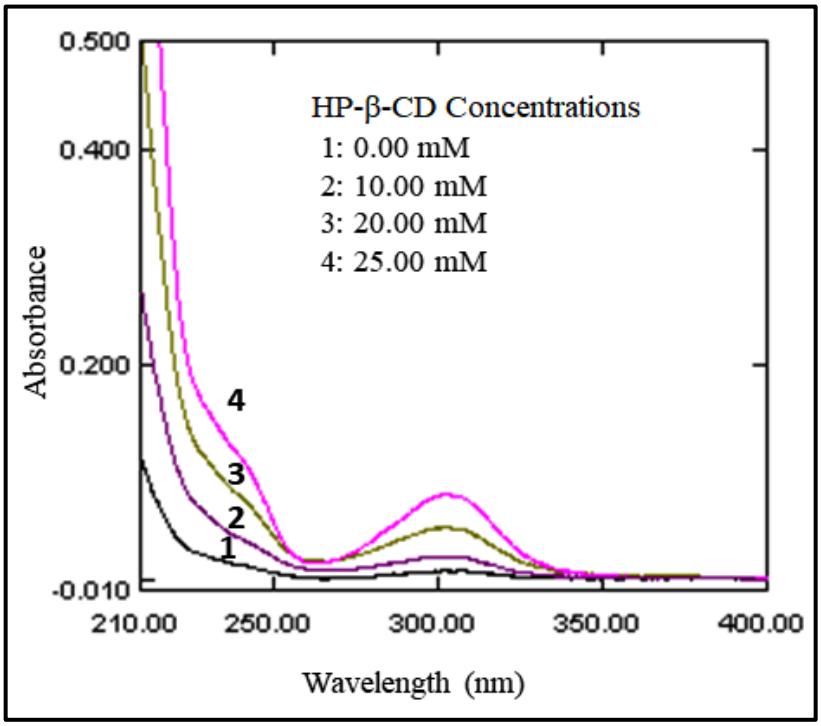

Figure 6.2: UV absorption spectra $Ana_{C15:3}$ in phosphate buffer pH 6.8 at different HP-β-CD concentrations: (1) 0.00 mM, (2) 10.00 mM, (3) 20.00 mM and (4) 25.00 mM

6.3.3 Preparation of Anacardic Acid/HP-β-CD inclusion complex

The $Ana_{C15:3}$-ICs were formulated using the co-evaporation method, and the effects of different variables on complexation efficiency were also investigated. It was clear from the results that the molar ratio of $Ana_{C15:3}$ (guest) and HP-β-CD (host) significantly affects the preparation of the inclusion complex. Enhancement in the complexation efficiency was observed with an increase in the molar ratio of HP-β-CD to $Ana_{C15:3}$ up to 2:1 which could be ascribed to the more number of host molecules available to accommodate the $Ana_{C15:3}$ molecules (Yildiz, Celebioglu et al. 2018). The effect of reaction temperature was also studied and had a positive impact on entrapment efficiency up to 45°C while

further increase in temperature did not show a significant increase. The reaction time and stirring speed were also optimized and found to be 2 h and 500 rpm, respectively. The present study revealed 2009 times enhancement in the solubility of $Ana_{C15:3}$ /HP-β-CD inclusion complex (38.17±0.38 mM) than $Ana_{C15:3}$ (0.019±0.005 mM) in pure water at 25°C.

6.3.4 Phase solubility study

Phase solubility study of $Ana_{C15:3}$ and $Ana_{C15:3}$ -IC was conducted in phosphate buffer (pH 6.8) at different temperature conditions *viz.* 25, 35, and 45°C (Figure 6.3). The solubility of $Ana_{C15:3}$ continued to increase with the increasing concentration of HP-β-CD and might be attributed to the more and more inclusion of $Ana_{C15:3}$ in the cavity of HP-β-CD. The driving force of inclusion complex formation is non-covalent interactions, out of which dipole-dipole interaction plays a key role in releasing high energy water molecules from the HP-β-CD cavity into the solvent media (Ol'khovich, Sharapova et al. 2017). It may be stipulated that with an increase in HP-β-CD concentration, more $Ana_{C15:3}$ molecules enter the HP-β-CD cavity which in turn increases the overall solubility of the $Ana_{C15:3}$. Enhanced solubility observed at higher temperatures could be attributed to the enhanced intrinsic solubility of $Ana_{C15:3}$ at higher temperatures (Xu, Zhang et al. 2017). Phase solubility diagram (Figure 6.3) was plotted and found to be linear, indicating A_L type as per Higuchi and Connors (Jagtap and Chandrakant 2018).

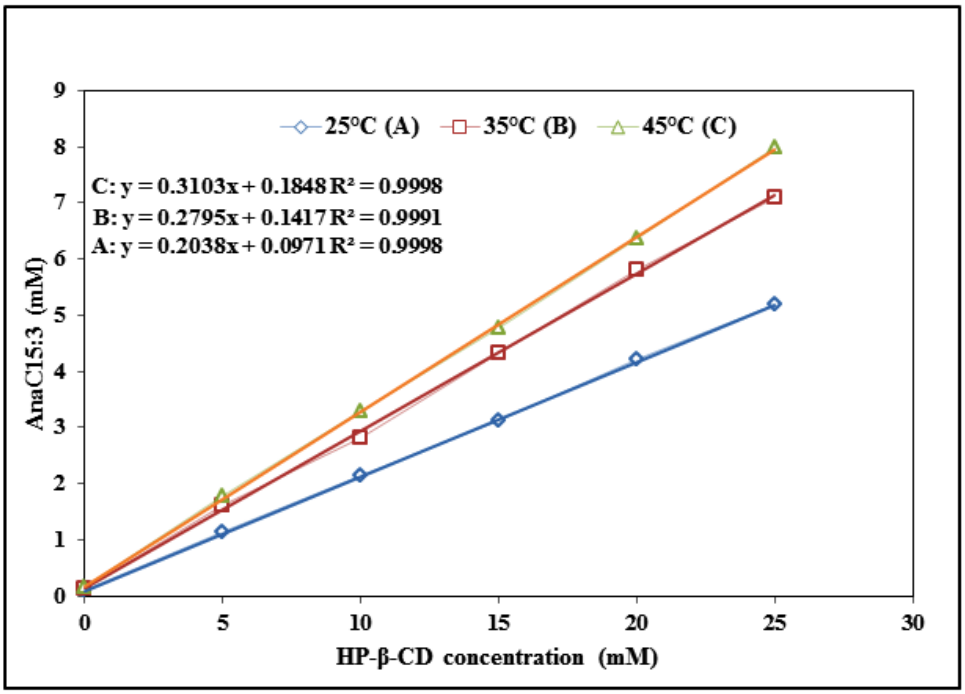

Figure 6.3: Phase solubility diagram of $Ana_{C15:3}$ as a function of HP-β-CD concentrations in phosphate buffer pH 6.8 at different temperatures (A) 25˚C, (B) 35˚C and (C) 45˚C.

Since the slope of the plot is <1, therefore it can be predicted that solubility enhancement might be attributed to the development of the first-order complex of $Ana_{C15:3}$ with HP-β-CD molecule, and also stoichiometry of the complex was assumed to be 1:1. The stability constant is of great importance, as it indicates the drug delivery applications possibility of inclusion complexes (Sursyakova, Levdansky et al. 2019). Considering the data obtained from phase solubility diagrams, the stability constants (K) of the $Ana_{C15:3}$-IC was calculated using Eqn. (1). The stability constants (K) obtained from phase solubility plots were 2830, 2750, and 2647 M^{-1} at temperatures 25, 35, and 45°C, respectively (Table 6.2). The results of the stability constants were between 200-5000$M^{-1,}$ demonstrating its stability and also suitability for improving solubility and bioavailability of the poorly water-soluble drugs (Ol'khovich, Sharapova et al. 2019).

Table 6.2: Various parameters for calculation of stability constant

Temp (°C)	Slope	Intrinsic Solubility (S_0) (mM)	Intercept	K (M^{-1})	Correlation Coefficient (R^2)
25	0.2038 ± 0.058	0.09	0.0971	2830	0.9998
35	0.2795 ± 0.077	0.141	0.1417	2750	0.9991
45	0.3103 ± 0.091	0.17	0.1848	2647	0.9998

Inverse relation of stability constant was found with temperature indicating the formation of inclusion complex to exothermic process, and stability of the complex reduces with an increase in temperature. It was observed that HP-β-CD at a concentration of 25 mM, the $Ana_{C15:3}$ solubility increases from 0.09 Mm to 5.18 mM indicating an approximately 58 folds' increase in solubility in pure phosphate buffer (pH 6.8).

6.3.5 Fourier transform infrared spectroscopy (FT-IR)

The formation of inclusion complexes of drugs with cyclodextrins can be easily assessed using FT-IR spectroscopy. This technique helps in determining the change in the bands of vibrations of the individual moiety in the process of complex formation (Gao, Bie et al. 2019). Inclusion complex formation is generally identified by a change in intensity, disappearance, and widening as well as shifting of peaks (Mangolim, Moriwaki et al. 2014). The FT-IR spectra of $Ana_{C15:3}$, HP-β-CD, physical mixture, and $Ana_{C15:3}$-IC are shown in Figure 6.4.

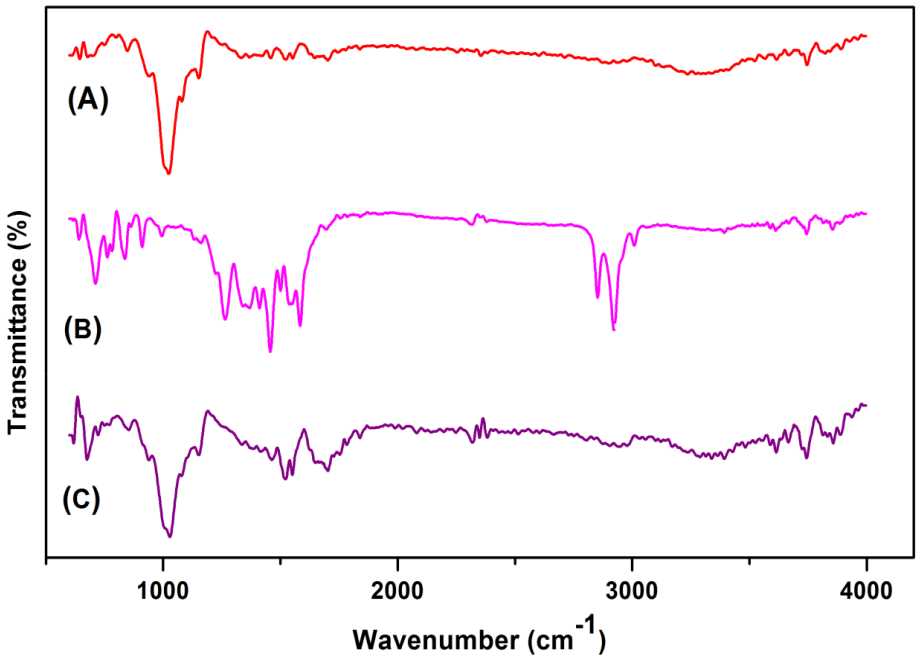

Figure 6.4: The FT-IR spectra of HP β-CD (A), $Ana_{C15:3}$ (B), and inclusion complex (C).

The FT-IR spectra of HP-β-CD showed the presence of peaks at 3600–3000 cm^{-1} (O-H stretching vibration), 1038 cm^{-1} (C=O stretching vibration), and 2917 cm^{-1} (C-H stretching vibrations). The FT-IR spectra of $Ana_{C15:3}$ revealed the presence of peaks at 3420 and 1304 cm^{-1} (Ar-OH), 3400-2400, 1645 cm^{-1} and 1304 cm^{-1} (-COOH), 3009 cm^{-1} (Ar-H and vinyl-H), 2924 and 2849 cm^{-1} (aliphatic C-H), 1607 cm^{-1} (aliphatic C=C), and 1446 cm^{-1} (aromatic C=C). The inclusion complex revealed a distinct FT-IR spectrum with the absence of absorption peaks at 2400-3400 cm^{-1}. The loss of aromatic peaks of $Ana_{C15:3}$ in the inclusion complex could be an indication of the inclusion of $Ana_{C15:3}$ inside the HP-β-CD cavity. Moreover, most of the peaks of $Ana_{C15:3}$ were observed to be smoothed, suggesting the prevalence of high intermolecular interaction between $Ana_{C15:3}$ and HP-β-CD. The IR band at 1636 cm^{-1} of the HP-β-CD relates to the water crystallization, which is absent in the inclusion complex spectra. This phenomenon is attributed to the replacement of water molecules inside the CD cavity with $Ana_{C15:3}$

molecules and thereby validating the inclusion complex formation (Rajendiran and Siva 2014).

6.3.6 X-ray diffraction (XRD) study

The formation of the inclusion complex was further confirmed by comparing the X-ray diffraction pattern of different samples. XRD analysis is prominently used as a tool to study cyclodextrins and their complexation with various compounds in powder form (Wang, Luo et al. 2014). Interaction between components in the formation of the inclusion complex can be assessed by comparing XRD patterns of individual compounds and inclusion complex. The appearance of new diffraction peaks, as well as the shift of drug (guest molecule) peaks or variations in their relative intensities, is the indications to confirm the formation of inclusion complex (Aytac, Kusku et al. 2016). The XRD patterns of $Ana_{C15:3}$, HP-β-CD, and $Ana_{C15:3}$-IC are shown in Figure 6.5.

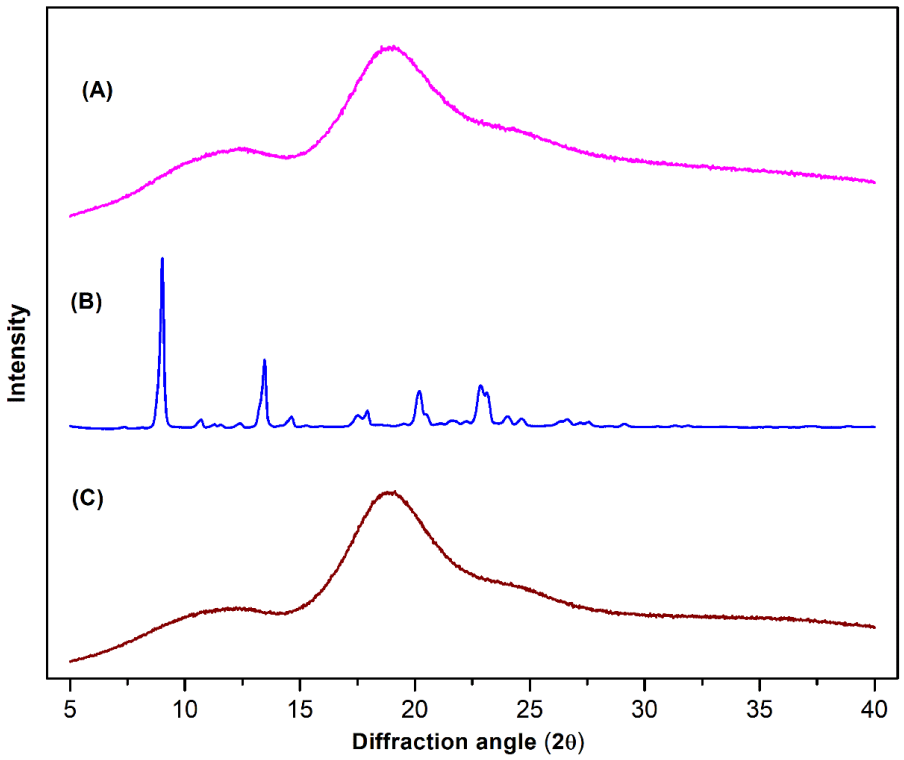

Figure 6.5: X-ray diffraction patterns of HP-β-CD (A), $Ana_{C15:3}$ (B), and inclusion complex (C).

Evidence of several peaks was observed in the XRD pattern of $Ana_{C15:3}$ (Figure 6.5-B) at diffraction angles (2θ) 9.02, 13.4, 17.9, 20.2, and 22.8, indicating crystallinity while XRD patterns of HP-β-CD did not show the presence of sharp peaks suggesting amorphous nature. However, HP-β-CD depicted broad diffraction peaks between 2θ = 15.52 and 22.12, suggesting a disordered crystal structure, which is a characteristic feature of amorphism. Furthermore, $Ana_{C15:3}$-IC displayed broad diffused peaks with decreased intensities as well as the complete absence of primary diffraction peaks corresponding to $Ana_{C15:3}$. This, in turn, provides conclusive evidence to favor the formation of inclusion complex consisting of solid phase and also transition from crystalline to amorphous form.

6.3.7 Differential scanning calorimetry (DSC)

DSC provides exhaustive data related to physical changes and therefore this technique has also been extensively used to investigate the interactions between drug, cyclodextrins, as well as inclusion complexes. Information regarding solid-state modifications and interaction among components can be obtained to compare the thermograms of individual compounds and complex (Li, Wang et al. 2018). The DSC thermal curves of $Ana_{C15:3}$, HP-β-CD, and inclusion complex are depicted in Figure 6.6. The DSC thermogram of $Ana_{C15:3}$ (Figure 6.6-B) revealed a wide peak at around 167°C, which is characteristic for the crystalline nature of the compound. DSC curve of HP-β-CD (Figure 6.6-A) shows an endothermic peak in the region between 33 to 113°C indicating amorphous nature which might be associated with the release of water from the cavity of HP-β-CD. In the thermogram of the inclusion complex (Figure 6.6-C), the complete absence of melting peaks corresponding to $Ana_{C15:3}$ was observed. However, a broad endothermic peak in the region 30 -132°C was seen, which an indication of the possible inclusion of $Ana_{C15:3}$ inside the HP-β-CD cavity.

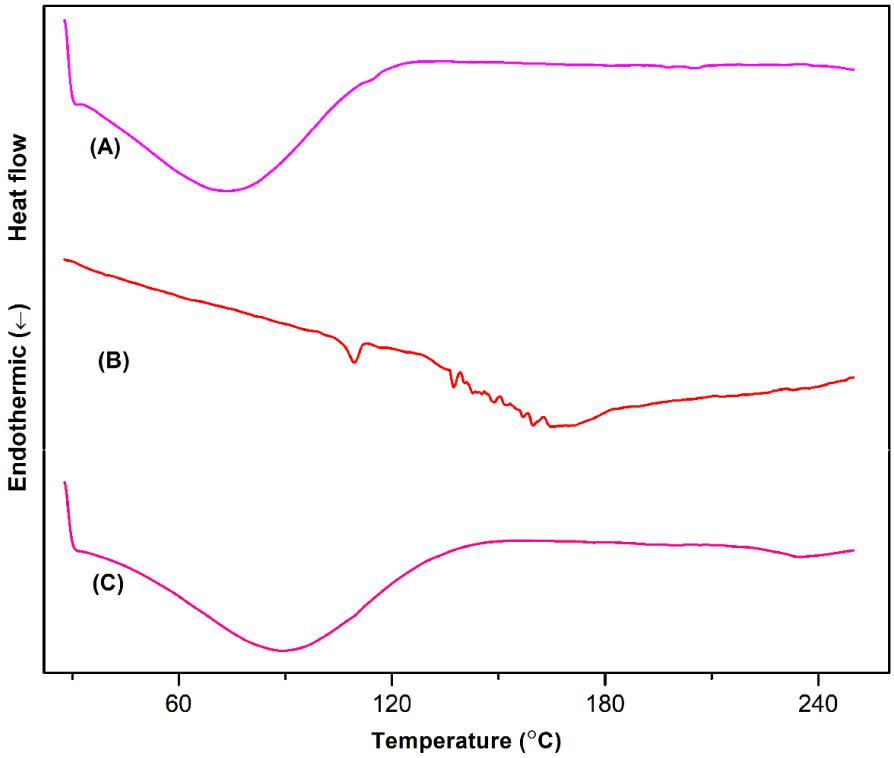

Figure 6.6: DSC thermograms of HP-β-CD (A), $Ana_{C15:3}$ (B), and the inclusion complex (C).

6.3.8 Scanning Electron Microscopy

Microscopic surface morphology was assessed using SEM, as the SEM analysis is ideal for quantitatively measuring the surface roughness and for visualizing the surface texture of the substance. The microscopic images of HP-β-CD and $Ana_{C15:3}$-IC are shown in Figure 6.7. The surface morphology of HP-β-CD revealed its spherical shape with the presence of the cavity inside while the inclusion complex (Figure 6.7-B) exhibited particles possessing a bulky prismatic shape. These pictures elucidated the difference between the HP-β-CD and the inclusion complex. Modification of the structures can be assumed as proof of the formation of a solid inclusion complex (Srinivasan and Stalin 2014).

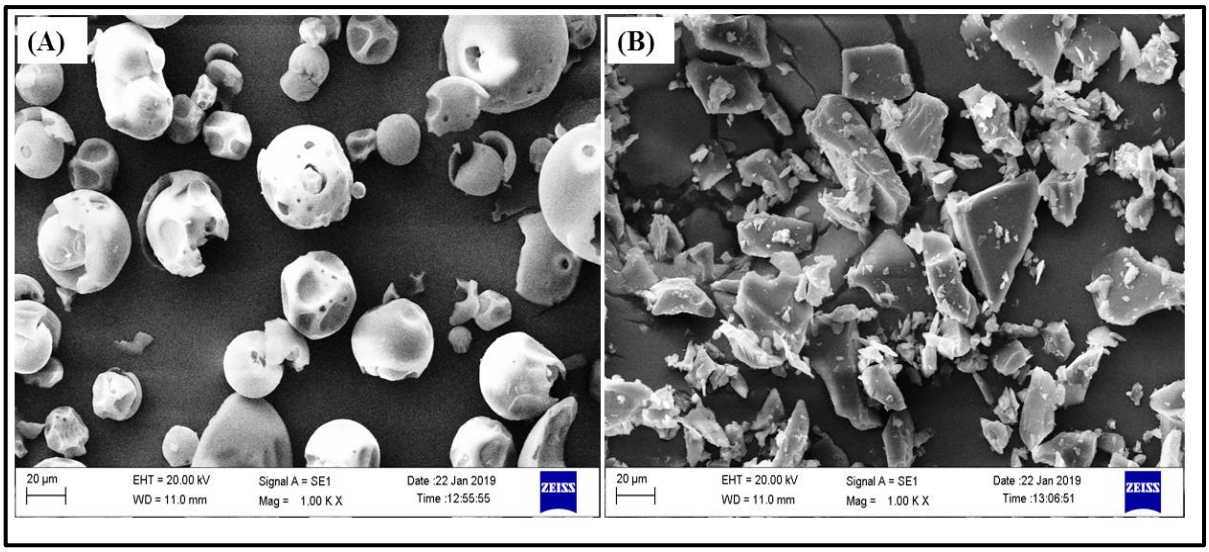

Figure 6.7: Scanning electron microscopy image of HP-β-CD (A) and Inclusion complex (B).

6.3.9 ^{1}H NMR (Proton) Spectroscopy

Formation of inclusion complex can be explained using ^{1}H NMR spectroscopy by considering changes in the chemical shift of protons of the $Ana_{C15:3}$ (guest) and HP-β-CD (host) molecules. However, changes in a chemical shift in this process are relatively small due to non-covalent interaction (Bulani, Kothavade et al. 2016). The inclusion behavior of $Ana_{C15:3}$ in HP-β-CD can be explained by comparing the chemical shift changes among ^{1}H spectra (Figure 6.8) of $Ana_{C15:3}$, HP-β-CD, and $Ana_{C15:3}$-IC (Table 6.3). The ^{1}H NMR spectra of $Ana_{C15:3}$ depicts aromatic moiety with absorption bands at ~7.012 ppm, ~6.503 ppm, and ~6.428 ppm due to H-4 (t), H-5 (d), and H-3 (d), respectively.

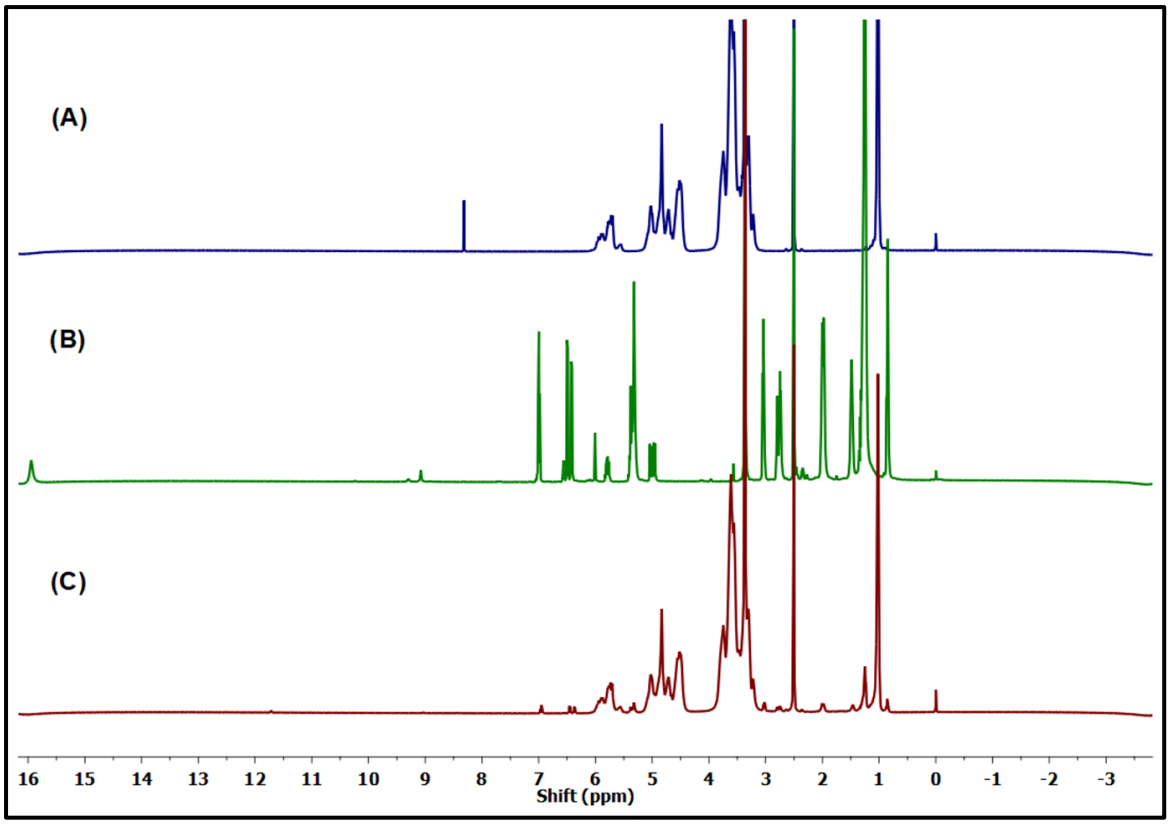

Figure 6.8: Comparative ^{1}H NMR spectrum of HP-β-CD (A), $Ana_{C15:3}$ (B), and inclusion complex (C).

Another absorption band was observed at 15.93, which was due to proton present in the –COOH group. The hydrogens present in double bonds of the alkyl chain showed absorption at different values of δ. Alkenyl protons showed absorption at 5.829-4.953, while methylene (CH_2) absorptions were observed at ~3.052, ~2.804, ~2.015, and ~1.484. Aliphatic CH_2 showed absorption at δ = 1.252. As demonstrated in Figure 6.8, the majority of the variations of chemical shifts of $Ana_{C15:3}$ (Figure 6.8-B) were in the aromatic and aliphatic region, which was distinct from the variation of HP-β-CD. The chemical shifts of HP-β-CD (Figure 6.8-A) were observed at δ values 5.87 due to H_1, 4.84 due to H_3, 3.74 due to H_5 & H_6, 3.61 due to H_2, and 1.02 due to the CH_3 group. All the characteristic chemical shifts of HP-β-CD and $Ana_{C15:3}$ were present in the proton NMR spectra of the $Ana_{C15:3}$ inclusion complex (Figure 6.8 C) except the absorption band of the

–COOH group of $Ana_{C15:3}$ which was observed in spectra $Ana_{C15:3}$ at δ value of 15.93. This indicates the possible inclusion of $Ana_{C15:3}$ into the HP-β-CD cavity.

Table 6.3: Variation of the ^1H NMR chemical shifts (δ /ppm) of $Ana_{C15:3}$ and HP-β-CD in inclusion complex formation.

Compound	Proton	δ (Free)	δ (Complex)	Δ δ
Anacardic Acid ($C_{15:3}$)	H_4	7.012	6.969	0.043
	H_5	6.503	6.455	0.048
	H_3	6.428	6.374	0.054
	Aliphatic (Alkenyl proton)	5.829	5.937	-0.108
	Methylene CH_2	3.052	3.034	0.018
	Aliphatic CH_2	2.804	2.792	0.012
	Aliphatic CH_2	1.484	1.472	0.012
HP-β-CD	H_1	5.874	5.828	0.046
	H_3	4.836	4.833	0.003
	H_5	3.742	Overlapped with HP-β-CD	
	H_6	3.745	Overlapped with HP-β-CD	
	H_2	3.613	3.632	-0.019
	CH_3	1.022	Overlapped with HP-β-CD	

6.3.10 Antimicrobial Activity

As per the results obtained from MIC assay against *S. aureus*, both $Ana_{C15:3}$ alone and $Ana_{C15:3}$-IC were effective against planktonic bacteria. The MIC value of both free $Ana_{C15:3}$ and $Ana_{C15:3}$-IC was 0.78 µg/mL indicating that the complexation process of $Ana_{C15:3}$ with HP-β-CD does not alter the antibacterial activity of $Ana_{C15:3}$ against the planktonic *S. aureus* rather it maintains the antibacterial activity as reported earlier (Teodoro, Gontijo et al. 2017). Maintaining the efficacy of drugs while developing a novel formulation may also be considered as the foundation of other useful applications (Zhao, Wang et al. 2010). The unchanged MIC value upon complexation is not surprising

as, at this lower concentration of $Ana_{C15:3}$, its water solubility is somehow not affected significantly as only free $Ana_{C15:3}$ out of the inclusion complex is available for its activity. The antibacterial action of $Ana_{C15:3}$ is primarily due to the physical disruption of the bacterial cell membrane, however, it has also been reported to act via entering into the cytoplasmic membrane lipid bilayers and thereby disrupting energy converting systems such as electron transport system (ETS) as well as ATPase. $Ana_{C15:3}$ also inhibit bacterial resistance possibly due to its action on the extracytoplasmic region and thereby avoiding cellular pump based resistance mechanisms (Parasa, Tumati et al. 2011, Hamad and Mubofu 2015).

6.3.10.1 Effect of $Ana_{C15:3}$ and $Ana_{C15:3}$-IC on S. aureus biofilms

The anti-biofilm activity of free $Ana_{C15:3}$ and $Ana_{C15:3}$-IC on 48 h grown mature biofilm at different concentrations is displayed in Figure 6.9. At the highest concentration, both free $Ana_{C15:3}$ and $Ana_{C15:3}$-IC exhibited more than 80% biofilm reduction. It can be observed that at concentrations below MIC, the anti-biofilm activity of $Ana_{C15:3}$ and $Ana_{C15:3}$-IC does not reveal a significant difference while at concentrations above MIC value, the $Ana_{C15:3}$-IC displayed excellent biofilm dispersal potential and there was a significant difference between the activity of free and complexed $Ana_{C15:3}$. This could be attributed to the fact that at concentrations below MIC value, $Ana_{C15:3}$ shows better aqueous solubility, and hence, it exhibits biofilm dispersal potential similar to the complexed $Ana_{C15:3}$. Moreover, the treatment of biofilms requires a high dose of the drug (more than MIC value), and due to poor aqueous solubility of $Ana_{C15:3}$, it does not demonstrate enough potential at higher concentrations as the insoluble fraction does not get access to the biofilms. Moreover, the inclusion complex formation with HP-β-CD results in a drastic enhancement in water solubility of $Ana_{C15:3}$, and thereby, the $Ana_{C15:3}$-IC exhibits

better biofilm eradication potential at higher concentrations (Sajeevan, Chatterjee et al. 2018).

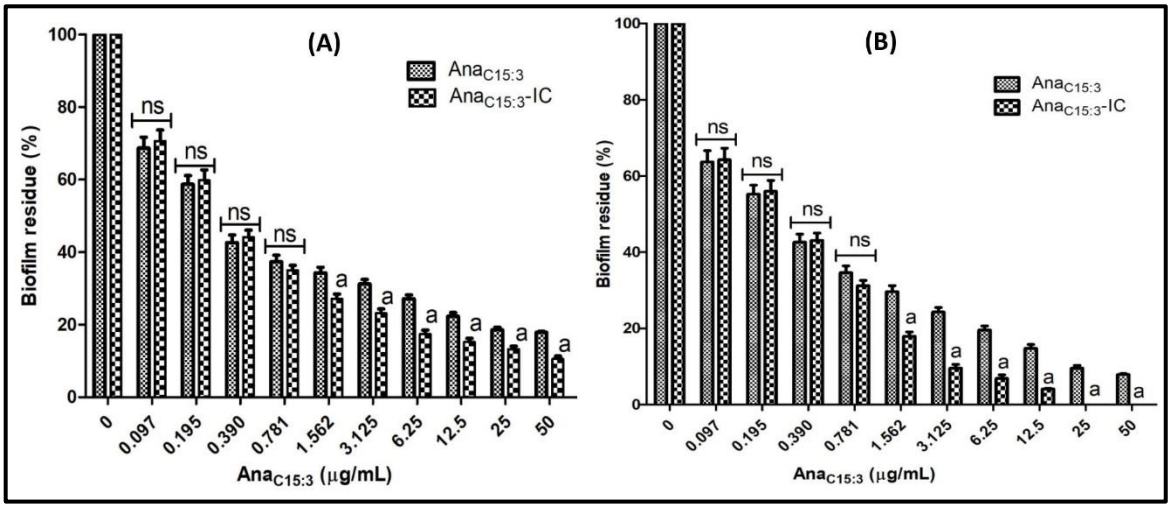

Figure 6.9: Disruption effect of free Ana$_{C15:3}$ and Ana$_{C15:3}$-IC on mature biofilm grown in 96 well plates. The graph depicts the percentage biofilm residue in response to different concentration of Ana$_{C15:3}$ and Ana$_{C15:3}$-IC. The study demonstrates a reduction of 48 h grown *S. aureus* biofilm on a single dose (Figure 6.9-A) and repeated dose for three recurrent days (Figure 6.9-B) of different Ana$_{C15:3}$ and Ana$_{C15:3}$-IC concentrations. The data represent a mean ± standard deviation (n=3). $^{a}p < 0.005$ as compared to Ana$_{C15:3}$ (Two way ANOVA followed by Bonferroni test). ns indicates the results are not significant as compared between the two groups. The viable count for the control experiment without Ana$_{C15:3}$ were $2.39\times10^{9} \pm 1.19\times10^{8}$ CFU/mL.

Furthermore, to explore the long term potential of Ana$_{C15:3}$ and Ana$_{C15:3}$-IC on mature biofilms, the anti-biofilm activity with consecutive treatment for 72 h was assessed. The free Ana$_{C15:3}$ exhibited biofilm reduction by 92.11% at the highest concentration (50 µg/mL) while Ana$_{C15:3}$-IC demonstrated complete biofilm dispersal at 25 µg/mL concentration. The improved biofilm dispersal potential of complexed Ana$_{C15:3}$ might be attributed to the enhancement of the aqueous solubility of Ana$_{C15:3}$, as discussed earlier. The other factors involved in such a phenomenon could be the slow release of Ana$_{C15:3}$ from the complex so that a gradient of the free and complexed drugs is maintained

throughout (Duarte, Alves et al. 2015). HP-β-CD is a bioadhesive and biocompatible biomaterial, which could have facilitated the adhesion of the inclusion complex with the biofilms (Aiassa, Zoppi et al. 2016).

6.3.10.2 Microscopic study of biofilm

Further confirmation of the antibiofilm potential of $Ana_{C15:3}$ and $Ana_{C15:3}$-IC was assessed on *S. aureus* biofilm grown for 48 h on the coverslip in culture plate (12 well). The data (

Table 6.4) depicts the biomass and thickness, which were derived from z stack CLSM images (Figure 6.10: A-C) using COMSTAT 2 software. The biofilms not receiving any treatment was considered as a control group which demonstrated the highest biomass (27.59 ± 2.2 $\mu m^3/\mu m^2$) and thickness (49.8 ± 4.17 µm). Furthermore, both free $Ana_{C15:3}$ and $Ana_{C15:3}$-IC displayed biofilm dispersal potential, but the complexed $Ana_{C15:3}$ showed better biofilm eradication and hence exhibited lower biomass and thickness.

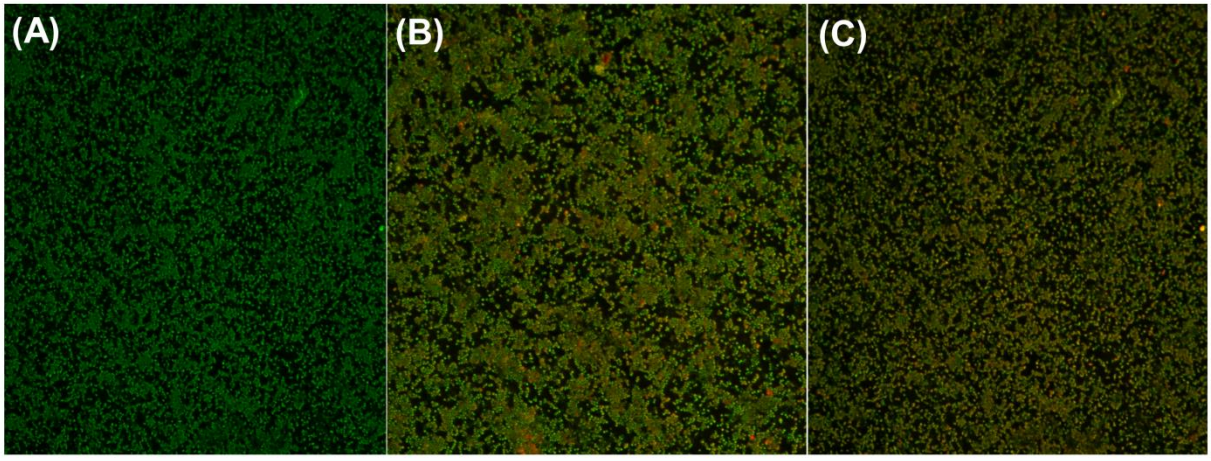

Figure 6.10: CLSM image of *S. aureus* biofilm formed on the coverslip surface with media supplementation. The images demonstrate dense biofilms formed without treatment (A) or with $Ana_{C15:3}$ (B) and $Ana_{C15:3}$-IC (C) treatment. The live cells are indicated by colored fluorescence while the dead cells appear as red colored cells. The control group demonstrates more green colored cells indicating live bacterial cells while the $Ana_{C15:3}$-IC treated group exhibited maximum red colored cells indicating dead cells.

Table 6.4: Biofilm parameters of *S. aureus* biofilms without treatment (control), $Ana_{C15:3}$, and $Ana_{C15:3}$-IC treatment.

	Biomass ($\mu m^3/\mu m^2$)	Thickness (μm)
Control (without treatment)	$27.59 \pm 2.2^{\#}$	$49.8 \pm 4.17^{\#}$
$Ana_{C15:3}$	$22.16 \pm 2.1^{*\#}$	$38.89 \pm 3.34^{*\#}$
$Ana_{C15:3}$-IC	$17.69 \pm 1.8^{*}$	$27.6 \pm 2.8^{*}$

* represents the significant difference in comparison with control (without treatment) biofilm, and # denotes a significant difference in comparison with $Ana_{C15:3}$-IC. ($p < 0.005$; Student's t-test). Data mentioned represented as mean ± standard deviation, of three replicated experiments.

$Ana_{C15:3}$ has earlier been reported to inhibit biofilm (Sajeevan, Chatterjee et al. 2018), the distinguishing property of $Ana_{C15:3}$ might be attributed to its unique features like it can penetrate the bacterial cell membrane and disrupt the lipid bilayers. $Ana_{C15:3}$ also interferes with the bacterial respiratory system by blocking its electron transport chain as well as NADH oxidase activity. Since $Ana_{C15:3}$ acts upon multiple targets and hence, it is effective against not only planktonic bacteria but also bacterial biofilms. Moreover, the complexation of $Ana_{C15:3}$ with HP-β-CD resolve the fundamental issue of water solubility and thereby making it potent even at lower concentrations. Thus, we evaluated the anti-biofilm activity on the glass surface, and the results indicated that $Ana_{C15:3}$-IC could potentially dismantle the adhered biofilm, which therefore suggested the new dimension in the treatment of biofilm-related infections (Tao, Hill et al. 2014, Gade, Patel et al. 2019). Biofilm forming bacteria communicate among its counterparts employing a specific mechanism known as quorum sensing. The potential of $Ana_{C15:3}$ to inhibit the quorum sensing makes it more effective in dismantling the bacterial biofilms (Asfour 2018).